Chapter 7

A Pictorial Representation of Product Operator Formalism: Non-Classical Vector Diagrams for Multidimensional NMR

DAVID G. DONNE* AND DAVID G. GORENSTEIN†

*Department of Molecular Biology
The Scripps Research Institute
10550 North Torrey Pines Road
La Jolla, CA 92037

†Sealy Center for Structural Biology and
Department of Human Biological Chemistry and Genetics
University of Texas Medical Branch
301 University Boulevard
Galveston, Texas 77555-1157

SUMMARY A complete pictorial representation for the product operator formalism has been developed to describe arbitrary multidimensional and multinuclear NMR experiments. A complete set of 16 multiple-headed vectors has been derived for a weakly-coupled two-spin ($I = 1/2$) system and extended to a three-spin system. The time evolution of chemical shift, scalar coupling, and the effects of pulses can then be easily visualized. More importantly, the concepts of coherence transfer, multiple quantum spectroscopy, and phase cycling are illustrated by examples such as 2D COSY, 2D INADEQUATE, DEPT, and sensitivity-enhanced HSQC.

7.1 Introduction

In the past two decades a variety of pulse NMR experiments have been developed with the aim of enhancing the information content or the sensitivity of NMR spectroscopy. For the design and analysis of new techniques three approaches have been pursued in the field of "spin engineering". Many of the original concepts were based on simplified classical or semi-classical vector models [1]. For the analysis of arbitrarily complex pulse experiments the density matrix theory was used, often at the expense of physical intuition [2-5]. A third approach, the product operator formalism [5-7], follows a middle course. It is founded on density operator theory but retains the intuitive concepts of the classical or semi-classical vector models. This formalism systematically uses product operators to represent the state of the spin system.

A close examination of product operator formalism reveals that the formalism weighs more on the density operator theory side and is still not intuitive enough for a clear understanding of complex NMR experiments to the average reader. On the other hand, the classical or semi-classical vector model has severe limitations. Although it can successfully describe heteronuclear 2D spectroscopy for weakly coupled spin systems and other polarization transfer experiments, it cannot explain homonuclear coherence transfer experiments (e.g. COSY) and experiments involving multiple quantum coherence (e.g. INADEQUATE). Furthermore, the latest triple-resonance NMR experiments have been developed almost exclusively based on the product operator formalism, and are far less intuitive to the general biophysics community. Attempts have been made to give graphical representation for the operators used in product operator formalism [6,8-10]. However, the original graphical scheme also uses energy levels and population distributions to represent some operator terms [6], making it unsuitable to following the fate of the spin system in a classical vector diagram manner. Some later approaches use multiple reference frames to follow spin states of different nuclei [9,10]. As a result the vector description of complex experiments are unnecessarily complicated and insights into phase cycling and frequency labeling during evolution are sacrificed in these representations [10]. A partial graphical representation using multiple-headed arrows to represent both in-phase and antiphase coherence transfer processes has also been reported in the literature to offer more insights into coherence transfer [8]. A correlated vector model, although not intended as a graphical representation of the product operator formalism, used similar multiple-headed arrows to analyze the HMQC experiment [11].

In this chapter, we will expand on the approaches followed in references [6,8] and describe a complete pictorial approach [12] to the description of multi-dimensional NMR experiments. In this approach, "non-classical" vectors similar to those used by Bazzo *et al.* [8] are first derived for all product operator terms for a two-spin ($I = 1/2$) system based on the population distribution of the spin state the operators represent. The pictorial description of evolution will then base its reasoning on the strict product operator formalism, while vectors mostly within the classical vector model framework will still be used to follow the fate of relevant spins in a weakly coupled spin ($I = 1/2$) system. Non-classical graphical extensions are added to account for time evolution of product operators only when necessary. For multispin systems, the pictorial representation of two-spin operators is extended to three or more spins. This approach can be used to follow any NMR experiment in an easily understandable way and offers an extension to the classical vector model to explain those experiments that cannot be followed using the classical vector model, as illustrated by its application to 2D COSY, INADEQUATE-2D, DEPT, and sensitivity-enhanced HSQC experiments.

7.2 Non-Classical Pictorial Representation of Base Operators

7.2.1 The Product operator formalism

In product operator formalism, the density operator of the spin system is expressed as a linear combination of base operator products. Cartesian base operators have found widespread use because they are very well suited for the description of pulse effects and time evolution. When multiple quantum coherence is involved, shift base operators prove to be more efficient. The Cartesian base operators are I_x, I_y, I_z, and $E/2$ (E is the unit operator). For a weakly coupled two-spin system ($I = \frac{1}{2}$), there are 16 product operators. These operators are: (1) zero-spin operator $E/2$; (2) one-spin operators I_{1x}, I_{1y}, I_{1z}, I_{2x}, I_{2y}, and I_{2z}; (3) two-spin operators $2I_{1x}I_{2x}$, $2I_{1x}I_{2y}$, $2I_{1x}I_{2z}$, $2I_{1y}I_{2x}$, $2I_{1y}I_{2y}$, $2I_{1y}I_{2z}$, $2I_{1z}I_{2x}$, $2I_{1z}I_{2y}$, and $2I_{1z}I_{2z}$. The one-spin operators are essentially classical. The two-spin operators (product operators) are non-classical in nature. We will first discuss how to represent these operators graphically using the two-spin system as an example. The time evolution of product operators and the pictorial interpretation will be discussed later. All discussions will be limited to spin 1/2 nuclei only.

7.2.2 Essence of the classical vector model

The essence of the classical vector model can be summarized as follows: in a Cartesian coordinate system, a vector along the *z*-axes represents polarization (population difference between the α and β spin states):

$$I_z = \frac{1}{2}(I^\alpha - I^\beta) \qquad [7.1]$$

and a vector within the *xy*-plane represents single-quantum coherence (Figure 7.1):

$$I_x = \frac{1}{2}(I^+ + I^-) \qquad [7.2]$$

$$I_y = \frac{1}{2i}(I^+ - I^-) \qquad [7.3]$$

Effects of pulses and chemical shift evolution can be described as rotation of vectors along *x*-, *y*-, or *z*-axis. Using the same principles, we can construct the graphical representation of product operators for a weakly-coupled spin system. The spin system is always treated in a heteronuclear manner, with non-selective pulses affecting all the spins in a homonuclear system. The arrows from different spins are labeled by their spin identities. In a weakly-coupled two-spin system, two single-headed arrows represent a one-spin operator. One double-headed arrow graphically describes one of the two operators in a two-spin product operator. The complete graphical representation of 16 operators in a weakly-coupled two-spin system is shown in Figure 7.2. For the simplicity of discussion, we will still refer to the multiple-headed arrow(s) associated with one operator term as a "vector", even though it is usually two or more single- or double-headed arrows combined and they transform as a whole.

7.2.3 Derivation of one-spin vectors

For one-spin operators I_{1z} and I_{2z} in a coupled two-spin system, we represent them as two parallel single-headed arrows along the *z*-axis (Figure 7.3) instead of energy levels showing pop-

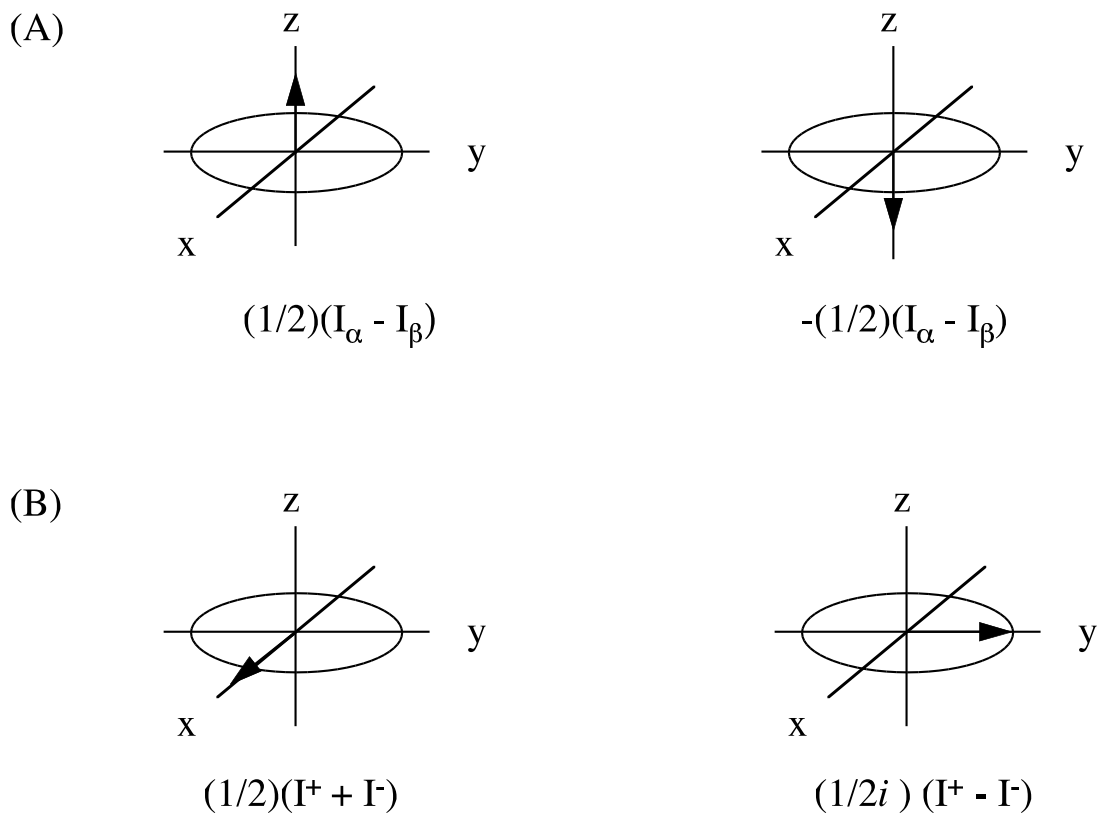

Figure 7.1: Classical vector representation of polarization and coherence for a one-spin system. (A) Polarization is represented by a vector on the *z*-axis. The direction of the vector depends on which state is more populated. (B) Coherence is represented by a vector on the *x*- or *y*-axis depending on which axis the magnetization is on.

ulation distributions [6]. Note that the sign convention is different than that in reference [6]. The representation for I_{1z} and I_{2z} in a two-spin system can be derived in the following way. In a one-spin system, the *z*-magnetization is described by a single vector along the *z*-axis because there is population difference between the two energy levels linked by a transition. This is shown in Figure 7.3A, where a filled circle represents a more populated state and an open circle represents a less populated state than the demagnetized saturated state [6]. In a two-spin system with spin 1 and spin 2, there are two different transitions for spin 1. One transition corresponds to the α state of spin 2 ($\alpha\alpha \rightarrow \beta\alpha$), and the other, the β state of spin 2 ($\alpha\beta \rightarrow \beta\beta$). At equilibrium, there is polarization across these two transitions for spin 1 and they are similar but different in nature because of the different spin state of spin 2. As a result we represent both I_{1z} and I_{2z} in a two-spin system by two parallel arrows each along the *z*-axis. This is illustrated for I_{1z} in Figure 7.3B. Again filled circles represent more populated states and open circles represent less populated states. Note that there is only polarization for spin 1 in Figure 7.3B and I_{1z} does not represent the equilibrium state of a two-spin system. The equilibrium population distribution for such a system is shown in Figure 7.3C.

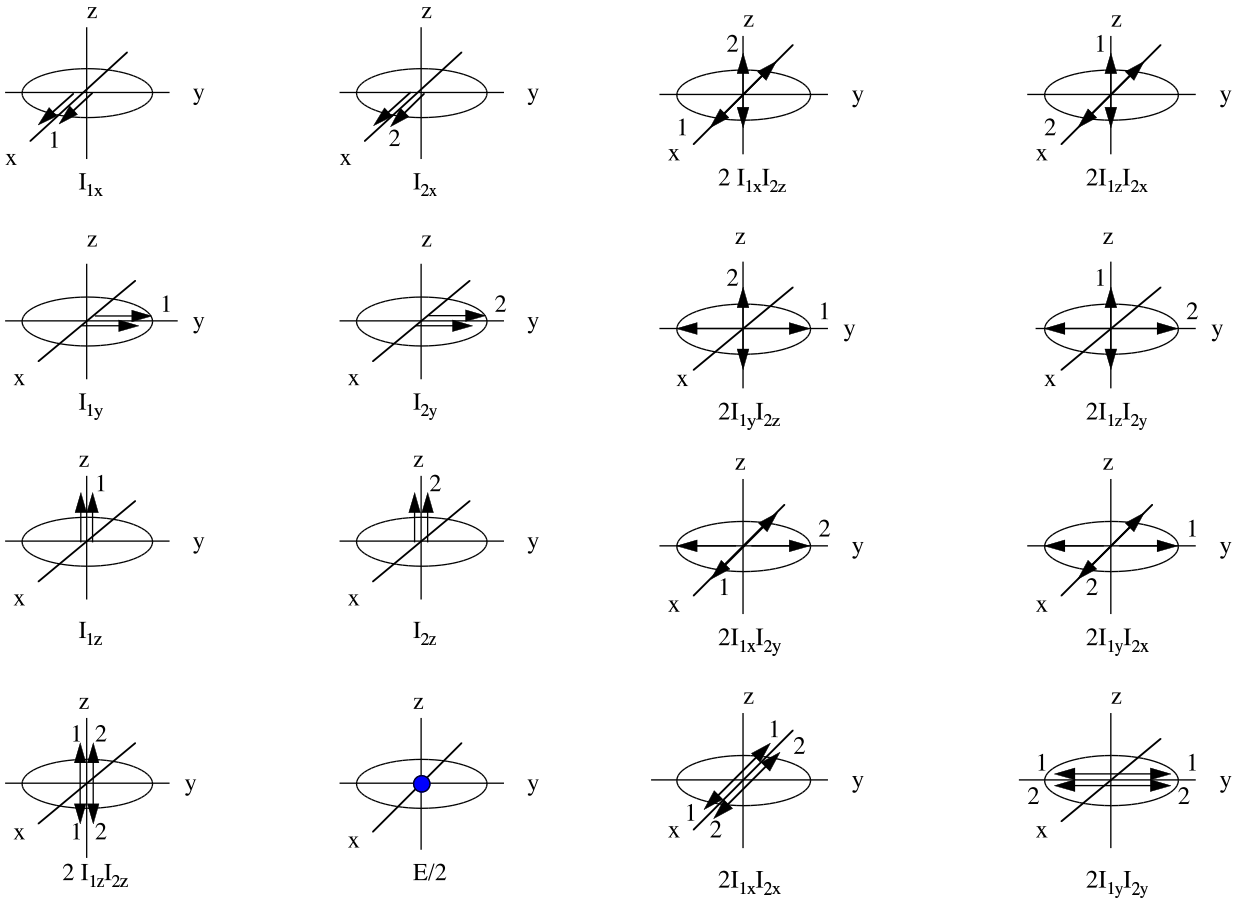

Figure 7.2: Non-classical vectors for the 16 operators of a weakly-coupled two-spin system. One-spin operators are represented by two single-headed arrows along their corresponding axes. Two-spin operators are represented by two double-headed arrows along their corresponding axes. The arrows are also labeled by their spin identities (i.e., spin 1 or spin 2). The zero-spin operator $E/2$ is included for completeness.

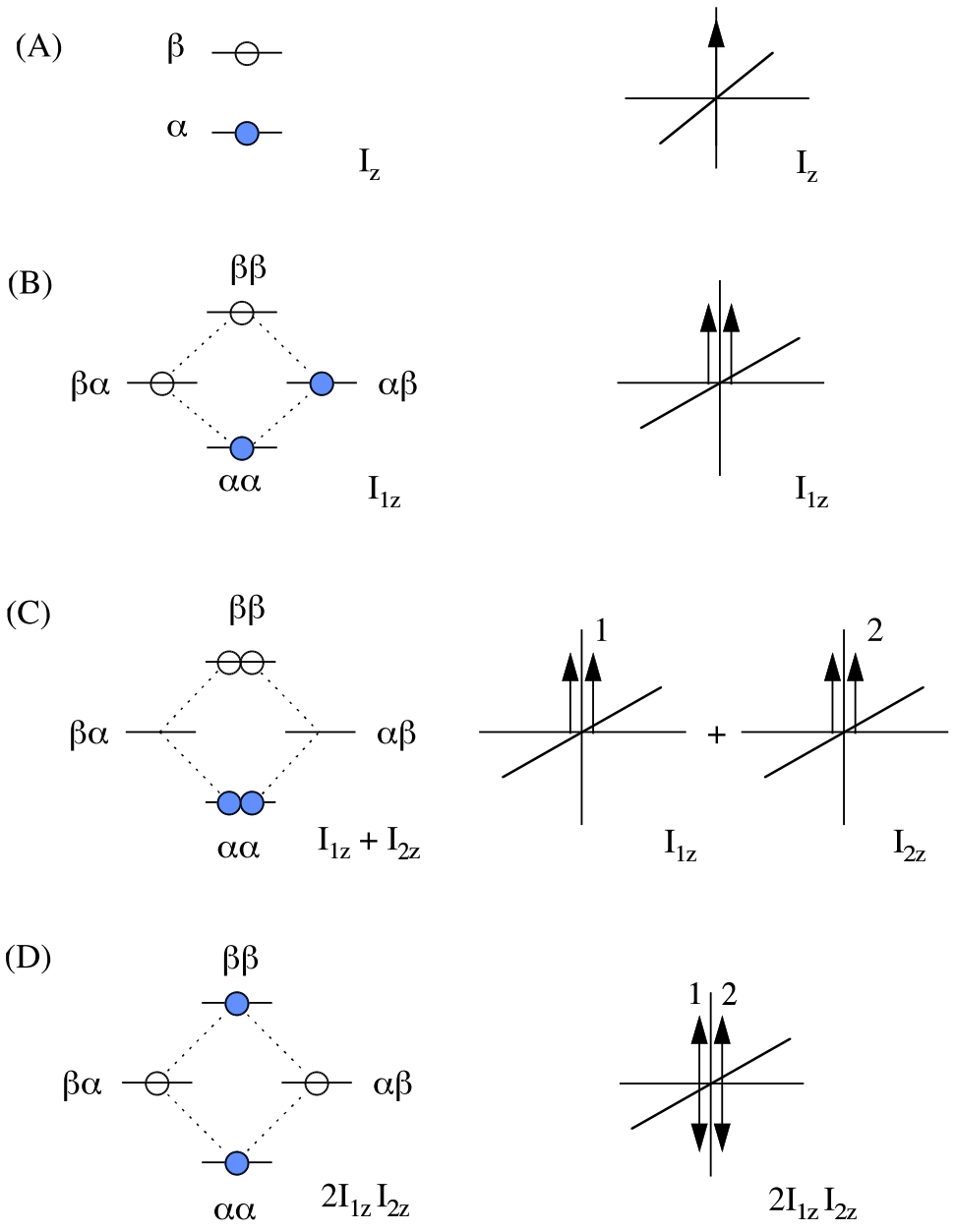

Figure 7.3: Relationship between vector representation and population distribution. Populations are symbolically represented by open circles for states that are depleted, filled circles for states that are more populated than in the demagnetized saturated state. (A) The vector I_z and its population distribution for a one-spin system. (B) The vector I_{1z} and its corresponding population diagram in a two-spin system. The two arrows come from the two transitions possible for spin 1. (C) The equilibrium state for a two-spin system. (D) Population diagram for vector $2I_{1z}I_{2z}$. For spin 1 the polarization is in opposite sense for the two transitions involved. Therefore the I_{1z} component in $2I_{1z}I_{2z}$ is represented by two arrows pointing to opposite directions giving a double-headed arrow when combined. The same applies to the I_{2z} component.

7.2.4 Derivation of two-spin vectors

We start the pictorial representation of two-spin operators from $2I_{1z}I_{2z}$. This operator describes longitudinal two-spin order of spin 1 and spin 2. The population distribution is shown in Figure 7.3D. It can be seen that the polarization of spin 1 is in opposite sense when spin 2 is in α state than in β state. This can be understood in the following way. In a weakly-coupled two-spin system, an ensemble of spin 1 can be divided into two halves. One half of spin 1 is associated with the α state of spin 2 and the other half is associated with the β state of spin 2. Then Figure 7.3D shows that the α state of spin 1 is more populated than the β state of spin 1 when its coupling partner spin 2 is in the α state. However, the α state of spin 1 is less populated than the β state of spin 1 when its coupling partner spin 2 is in the β state. Therefore we represent these two polarizations by two single-headed arrows with opposite directions. Together these two arrows form a double-headed arrow representing the polarization of spin 1. The situation is similar with spin 2 and it is also represented by a double-headed arrow. The two double-headed arrows for spin 1 and spin 2 combined together represent the product operator $2I_{1z}I_{2z}$ (Figure 7.3C). This can be better understood when expanding the operator term in the following way:

$$2I_{1z}I_{2z} = \frac{1}{2}(I_{1z}I_2^{\alpha} - I_{1z}I_2^{\beta}) + \frac{1}{2}(I_1^{\alpha}I_{2z} - I_1^{\beta}I_{2z}) \qquad [7.4]$$

It can be seen clearly that the population difference (*z*-magnetization) of one spin has opposite signs when the other spin (coupled to the first spin) is in a different spin state. Experimentally, the spin state represented by the vector $2I_{1z}I_{2z}$ is the one obtained in a Selective Population Inversion (SPI) experiment in a two-spin AX system. When the population across one transition of the A spin is inverted from its equilibrium state by a selective 180° pulse on only one transition of the A doublet, the polarization across only one of the X transitions is inverted, leaving both A and X in an antiphase state.

Now the vectors of the other two-spin product operators can be obtained based on rotational properties (Figure 7.4). Starting from $2I_{1z}I_{2z}$ a selective 90° *x*-pulse acting on spin 1 will give $2I_{1y}I_{2z}$, the antiphase *y*-magnetization on spin 1. A non-selective 90° *x*-pulse will generate $2I_{1y}I_{2y}$, a combination of zero-quantum coherence and double-quantum coherence. The non-classical vectors for other two-spin product operators can be derived similarly as shown in Figure 7.4. Finally, the zero-spin operator $E/2$, although not involved in the description of NMR experiments, is described by a sphere at the origin based on its symmetry properties.

7.3 Graphical Description of Time Evolution

7.3.1 Chemical shift evolution

For weakly-coupled spin systems, the density operator evolves under the Hamiltonian

$$\mathcal{H} = \sum_k \omega_k I_{kz} + \sum_k \sum_{k<l} \pi J_{kl}(2I_{kz}I_{lz}) \qquad [7.5]$$

where ω_k is the chemical shift frequency of nucleus *k* in the rotating frame. Because all terms in the Hamiltonian commute, we can follow the evolution caused by chemical shift and *J*-coupling separately in any arbitrary order. In the following discussion, we will use the symbolic notation by

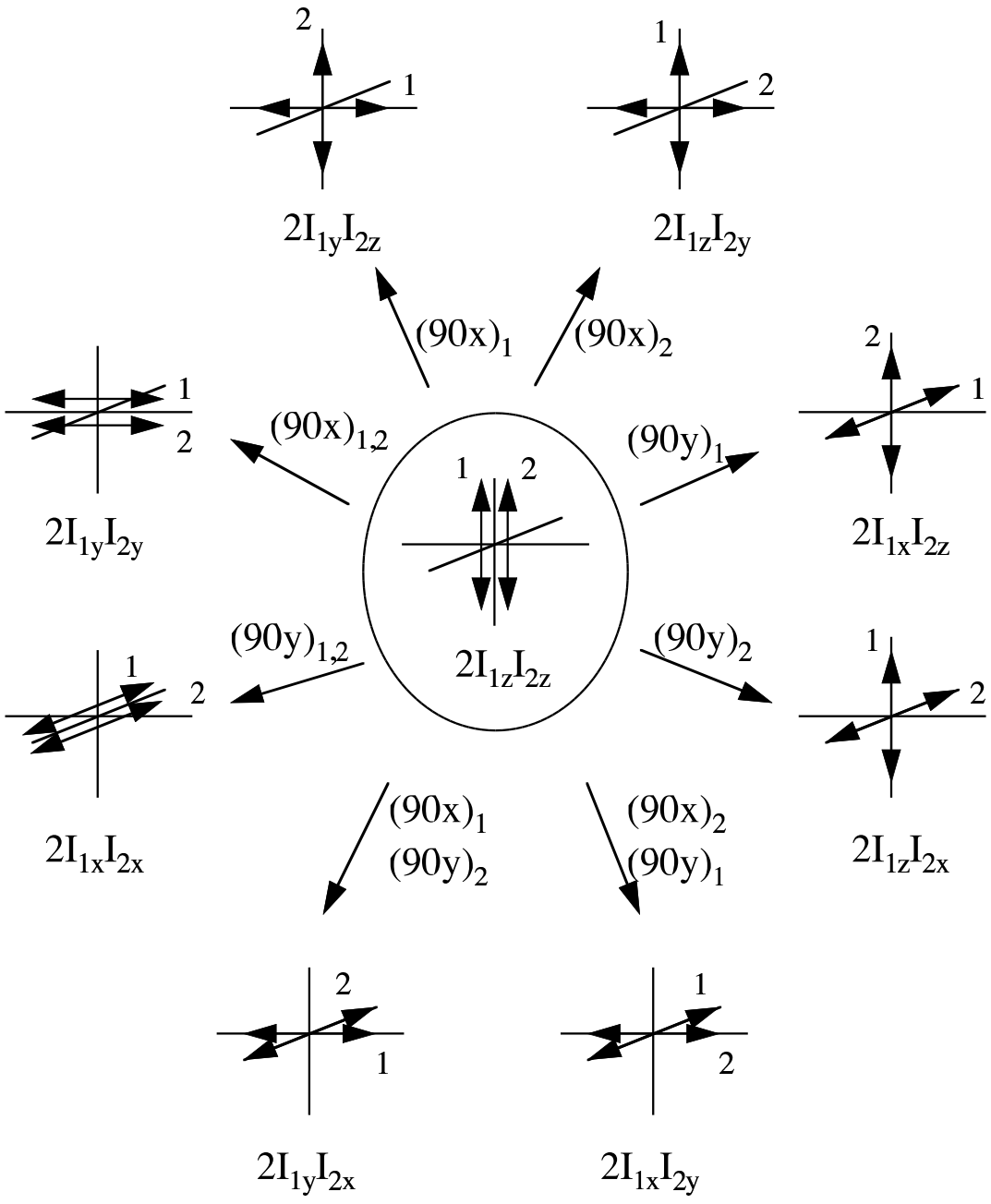

Figure 7.4: Derivation of two-spin vectors from $2I_{1z}I_{2z}$. The phase of the pulses is indicated by *x* and *y*. The numbers 1 and 2 for the pulses show the pulses are applied selectively on either spin 1, spin 2, or both.

Sørensen *et al.* [6] but use an opposite sign convention[1] to be consistent with the sign convention in the classical vector model.

In product operator formalism, the chemical shift evolution in a two-spin system is described by

$$I_{1x} \xrightarrow{\omega_1 \tau I_{1z}} I_{1x}\cos\omega_1\tau - I_{1y}\sin\omega_1\tau \quad [7.6]$$

$$I_{1y} \xrightarrow{\omega_1 \tau I_{1z}} I_{1y}\cos\omega_1\tau + I_{1x}\sin\omega_1\tau \quad [7.7]$$

$$I_{1y}I_{2z} \xrightarrow{\omega_1 \tau I_{1z}} I_{1y}I_{2z}\cos\omega_1\tau + I_{1x}I_{2z}\sin\omega_1\tau \quad [7.8]$$

The graphical scheme for chemical shift evolution of of in-phase vector I_{1y} is shown in Figure 7.5A, where we show both the overall vector after the evolution and its decomposed components. The decomposed *x*- and *y*-components are more helpful to understanding the spin physics when they belong to different coherence pathways in multiple pulse experiments. The graphical representation for chemical shift evolution of of antiphase vector $I_{1y}I_{2z}$ is shown in Figure 7.5B. Note that *J*-coupling between spin 1 and spin 2 is not considered (or decoupled) here and the two sub-vectors with the *xy*-plane evolve independently. After decomposition we have two antiphase vectors as a result.

Product operators with p transverse single spin operators are a superposition of multiple quantum coherence of orders $q = p - 2n$ $(n = 0, 1, 2, ...)$, where p is the number of transverse single spin operators in the product. The chemical shift evolution of multiple quantum terms can be described separately because the chemical shift Hamiltonians for different spins commute with each other. For example, for a product operator representing two-spin coherence, the chemical shift evolution is described by

$$2I_{1x}I_{2y} \xrightarrow{\omega_1 \tau I_{1z}} \xrightarrow{\omega_2 \tau I_{2z}} 2(I_{1x}\cos\omega_1\tau - I_{1y}\sin\omega_1\tau)(I_{2y}\cos\omega_2\tau + I_{2x}\sin\omega_2\tau) \quad [7.9]$$

The graphical scheme for multiple quantum term $2I_{1x}I_{2y}$ is shown in Figure 7.5C, where ω_1 and ω_2 are precession frequencies of spin 1 and spin 2, respectively. The resulting vectors of the product term can be obtained by taking the projection of vectors for spin 1 and spin 2 and combining them to form four new vectors as shown in Figure 7.5C. The resultant vectors contain the chemical shift evolution effects of both spins because the evolution of both spins will modulate the amplitude of the overall vector. It should be emphasized that the Cartesian operators do not represent pure orders of multiple quantum coherence. However, they are well suited for our purpose to describe evolution effects in the time course of the pulse sequence.

7.3.2 Scalar coupling evolution

Scalar coupling (*J*-coupling) is the interaction between two spins through bonds and is one of the most important and exploited phenomena in multidimensional NMR. It is the origin of splitting of resonances in the NMR spectrum and its magnitude is a sensitive measure of torsional

[1] In the classical vector description of NMR experiments, the left-hand rule is often used, i.e., a 90° pulse on the *x*-axis will rotate the *z*-magnetization vector to the *y*-axis. In the more mathematics-oriented literature, the right-hand rule is often used, as in the case of reference [6]. Here we adopt the sign convention found in the classical vector models for smooth transition from classical vector models to non-classical vector models.

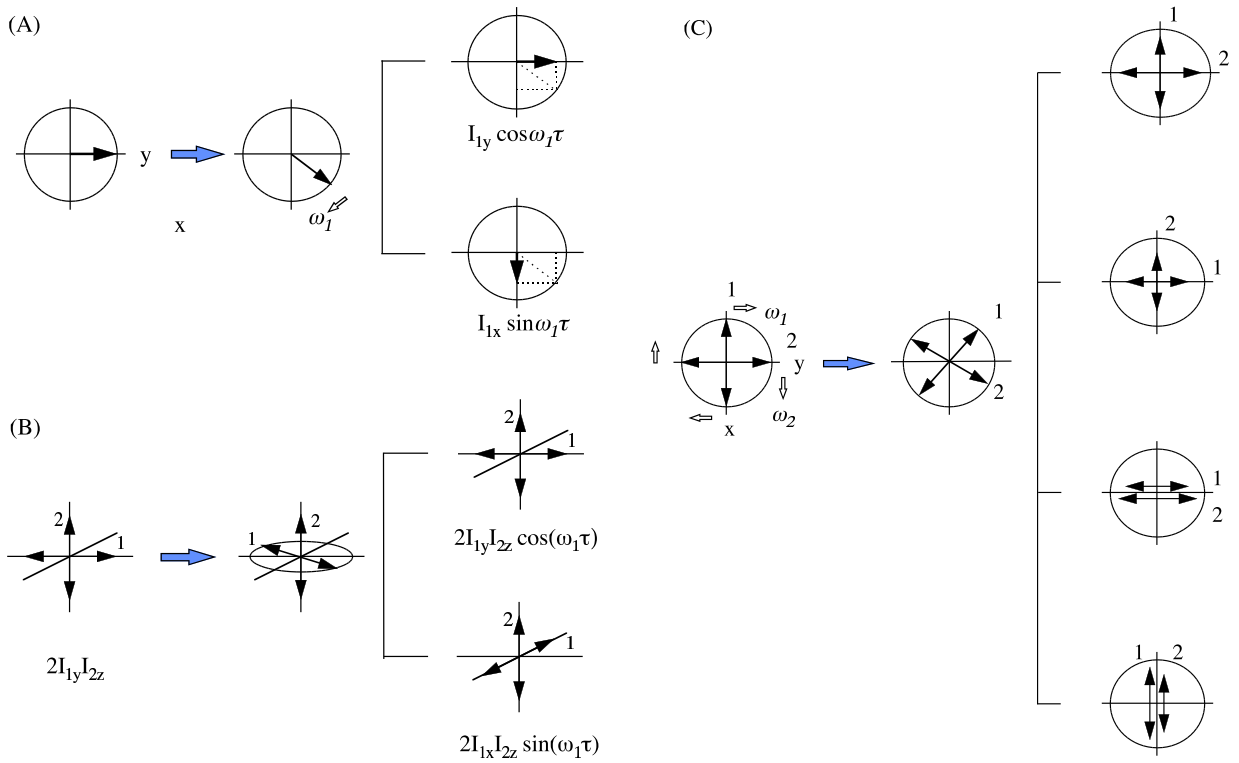

Figure 7.5: Vector representation of chemical shift evolution. (A) Chemical shift evolution of in-phase vector I_{1y} is shown in a conventional form and in a decomposed form. When evolution is emphasized the conventional form is more useful. When coherence selection or frequency labeling is emphasized the decomposed form proves more efficient. (B) Chemical shift evolution of antiphase vector $I_{1y}I_{2z}$. The two sub-vectors of spin 1 in the beginning representing the two halves of spin 1 corresponding to the α and β states of spin 2. The two sub-vectors evolve independently when *J*-coupling is not considered or decoupled. The final result is two antiphase vectors (in decomposed form) with the amplitude modulated by chemical shift of spin 1. (C) Chemical shift evolution of multiple-quantum vectors. Chemical shift evolution of spin 1 and spin 2 occurs independently. After decomposition into *x*- and *y*- components, four possible combinations of two vector projections are obtained.

angles in the molecule under investigation. Scalar coupling is also the basis of many important multidimensional coherence transfer experiments such as COSY and TOCSY. In the context of vector diagrams, it leads to the failure of the classical vector model. In the following the product operator description for weak scalar coupling along with the non-classical vector representation will be presented.

For weak coupling between two nuclei of spins $I = \frac{1}{2}$ the product operator rules are

$$I_{1x} \xrightarrow{\pi J_{12}\tau 2I_{1z}I_{2z}} I_{1x}\cos(\pi J_{12}\tau) - 2I_{1y}I_{2z}\sin(\pi J_{12}\tau) \quad [7.10]$$

$$I_{1y} \xrightarrow{\pi J_{12}\tau 2I_{1z}I_{2z}} I_{1y}\cos(\pi J_{12}\tau) + 2I_{1x}I_{2z}\sin(\pi J_{12}\tau) \quad [7.11]$$

$$2I_{1x}I_{2z} \xrightarrow{\pi J_{12}\tau 2I_{1z}I_{2z}} 2I_{1x}I_{2z}\cos(\pi J_{12}\tau) - I_{1y}\sin(\pi J_{12}\tau) \quad [7.12]$$

$$2I_{1y}I_{2z} \xrightarrow{\pi J_{12}\tau 2I_{1z}I_{2z}} 2I_{1y}I_{2z}\cos(\pi J_{12}\tau) + I_{1x}\sin(\pi J_{12}\tau) \quad [7.13]$$

In Equation 7.10, the in-phase term $I_{1x}\cos(\pi J_{12}\tau)$ will give two in-phase peaks (cosine modulation on I_{1x}) separated by J Hz after Fourier transformation, while the antiphase term $2I_{1y}I_{2z}\sin(\pi J_{12}\tau)$ is not observable because

$$Tr[(I_1^+ + I_2^+)(2I_{1y}I_{2z}\sin(\pi J_{12}\tau))] = 0 \quad [7.14]$$

This can also be clearly seen from the vector representation of the antiphase terms: the positive x- or y-component has equal magnitude as the negative counterpart and will cancel with each other. In Equation 7.12, the in-phase term $I_{1y}\sin(\pi J_{12}\tau)$ will give two antiphase peaks (sine modulation on I_{1y}) separated by J Hz after Fourier transformation, while the antiphase term $2I_{1x}I_{2z}\cos(\pi J_{12}\tau)$ is still not observable. It should be emphasized that an antiphase term is always unobservable directly. However, if J-coupling is present, the antiphase term will be converted to in-phase magnetization by scalar coupling as described in Equations 7.12 and 7.13, thus giving observable signals originating from the antiphase terms. It can also be easily seen that the in-phase magnetization will lead to antiphase magnetization and vice versa due to scalar coupling from Equations 7.10–7.13. This is in contrast to the evolution of chemical shifts and/or pulses in that the resulting vectors can not be obtained by simply rotating the starting vector.

The graphical representation for scalar coupling is shown for $2I_{1x}I_{2z}$ (Figure 7.6A) and I_y (Figure 7.6B). Starting from antiphase vector $2I_{1x}I_{2z}$, only spin 1 will evolve under the influence of scalar coupling due to the local field from the z-magnetization of spin 2 [10, 11]. After time τ, the transverse components have moved towards each other and can be projected to the x- and y-axes to give in-phase and antiphase components as shown in Figure 7.6A. Note that the decomposition is unique because only the base vectors in Figure 7.2 are allowed in the representation. Similarly, the in-phase vector $2I_{1y}$ will evolve to give both in-phase and antiphase components as shown in Figure 7.6B. It can be thought of as the in-phase magnetization I_y is partially converted to the antiphase magnetization $2I_{1x}I_{2z}\sin(\pi J_{12}\tau)$ and the remaining in-phase magnetization is $I_{1y}\cos(\pi J_{12}\tau)$. Essentially, the magnetization is oscillating between in-phase and antiphase vectors. The difference between the classical model and the non-classical model with respect to spin coupling is that only one spin (the one tipped down to the xy-plane) is included in the classical model, while the spin states of both spins are included in the non-classical model. Multiple-quantum coherence does not evolve under active coupling, the effect is shown in Figure 7.6C.

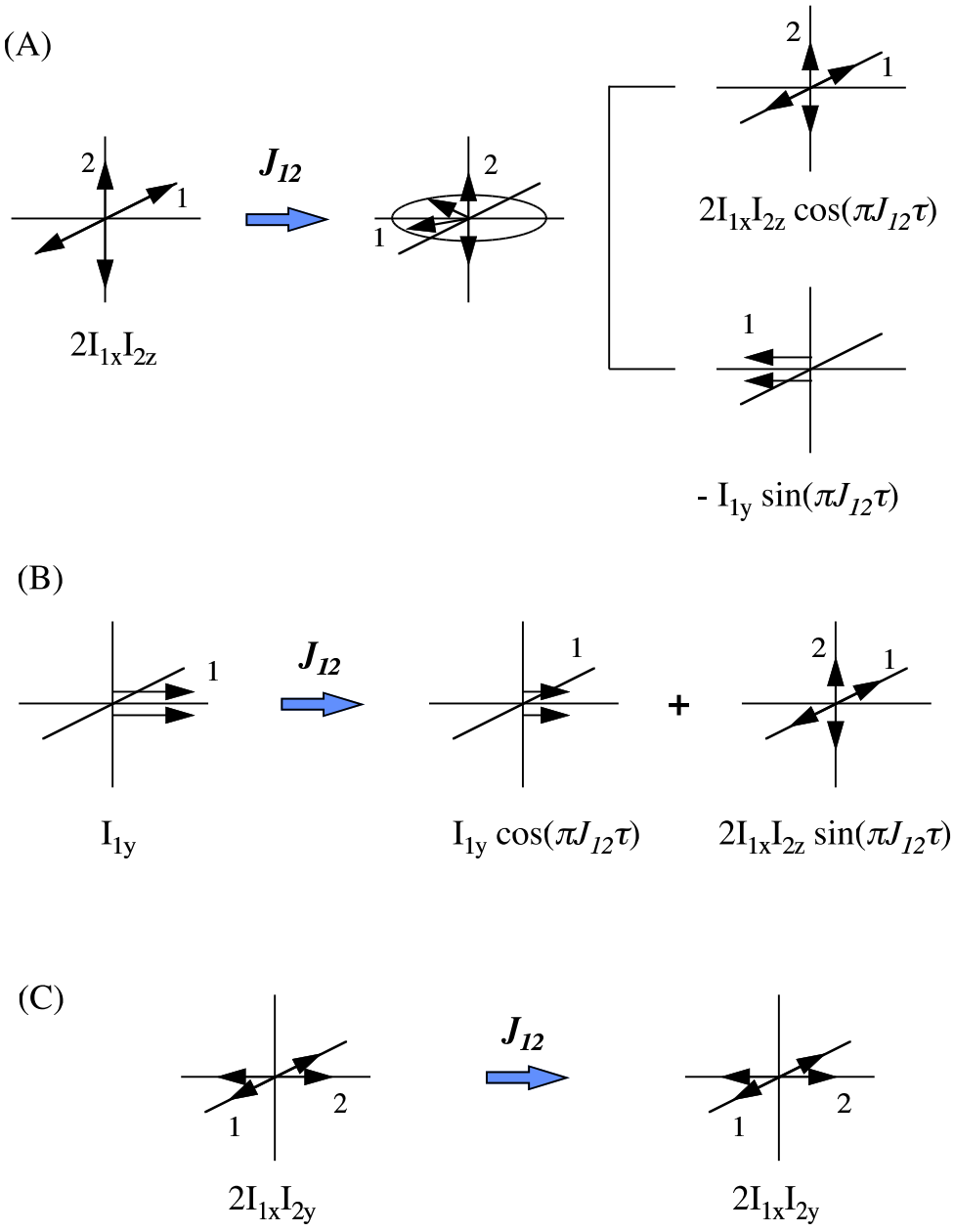

Figure 7.6: Scalar coupling evolution of product operators. (A) Scalar coupling evolution of antiphase vector $2I_{1x}I_{2z}$. Only the transverse vector from spin 1 evolves due to the local field produced by spin 2. After decomposition, it gives rise to sine modulated in-phase vector $-I_{1y}\sin(\pi J_{12}\tau)$ and cosine modulated antiphase vector $2I_{1x}I_{2z}\cos(\pi J_{12}\tau)$. (B) Scalar coupling evolution of in-phase vector I_{1y}. Under scalar coupling it gives rise to cosine modulated in-phase vector $I_{1y}\cos(\pi J_{12}\tau)$ and sine modulated antiphase vector $2I_{1x}I_{2z}\sin(\pi J_{12}\tau)$. (C) Multiple quantum coherence does not evolve under the active scalar coupling involved.

7.3.3 Effects of pulses

With all the vectors developed for all 16 operators for a two-spin system, it is straightforward to visualize the effect of pulses in any NMR experiment. Figure 7.7 shows the results of a hard 90° pulse of phase *x* on various starting vectors. In Figure 7.7A, *z*-magnetization I_{1z} is converted to transverse magnetization I_{1y} as in the classical vector model. In Figure 7.7B, antiphase vector $2I_{1y}I_{2z}$ is transformed to antiphase vector $2I_{1z}I_{2y}$. Now the transverse magnetization resides on spin 2 as opposed to on spin 1 before the pulse. This is the coherence transfer step, which occurs in many multi-dimensional NMR experiments such as COSY and HETCOR. In Figure 7.7C, antiphase magnetization $2I_{1x}I_{2z}$ is converted to multiple quantum coherence $2I_{1x}I_{2y}$ as readily visualized with our model, because vector components from both spin 1 and spin 2 are within the *xy*-plane. This process plays a central role in multiple quantum spectroscopy experiments such as INADEQUATE and HMQC. Finally, after multiple quantum coherence has been allowed to evolve during the incremented time period, it has to be converted to single quantum coherence for detection. This is readily visualized in Figure 7.7D, where one of the vector components is rotated by the 90°_x pulse to the *z*-direction, leaving only the transverse magnetization from the other spin for detection with antiphase being converted to in-phase magnetization under J evolution. In short, the four rotations described in Figure 7.7 summarize all important roles of radio-frequency pulses in modern NMR: preparation of transverse magnetization (Figures 7.7A and 7.7C), mixing of magnetization from different spins (Figure 7.7B), and conversion to single-quantum magnetization for detection (Figure 7.7D).

7.3.4 Vector representation of three-spin systems

The pictorial representation of product operators for systems with three or more spins ($I = \frac{1}{2}$) can be derived based on the analysis for a two-spin system. For any in-phase term, we will represent the overall magnetization vector as one single-headed arrow. For antiphase operator terms, the *z*-magnetization for a specific spin will be described by only one double-headed arrow labeled as that spin along the *z*-axis. All the other transverse components in the product term will be represented by a double-headed arrow along their corresponding axes with spins also labeled (Figure 7.8). As will be shown later, this scheme is simple and sufficient to describe any recent multi-dimensional triple-resonance experiment.

7.4 Application of the Non-Classical Vector Model

In this section we will apply our vector model to describe some of the most important 2D and 3D experiments. First, the 2D homonuclear COSY [13] experiment will be analyzed. Two multiple quantum experiments, INADEQUATE-2D [14-16] and DEPT [17,18], will also be described using this vector model. Then an example of the sensitivity-enhanced experiments, sensitivity-enhance HSQC [22], will be described. The pulse sequences of these experiments are shown in Figure 7.9. Some fine points about using the new vector model will also be discussed when appropriate.

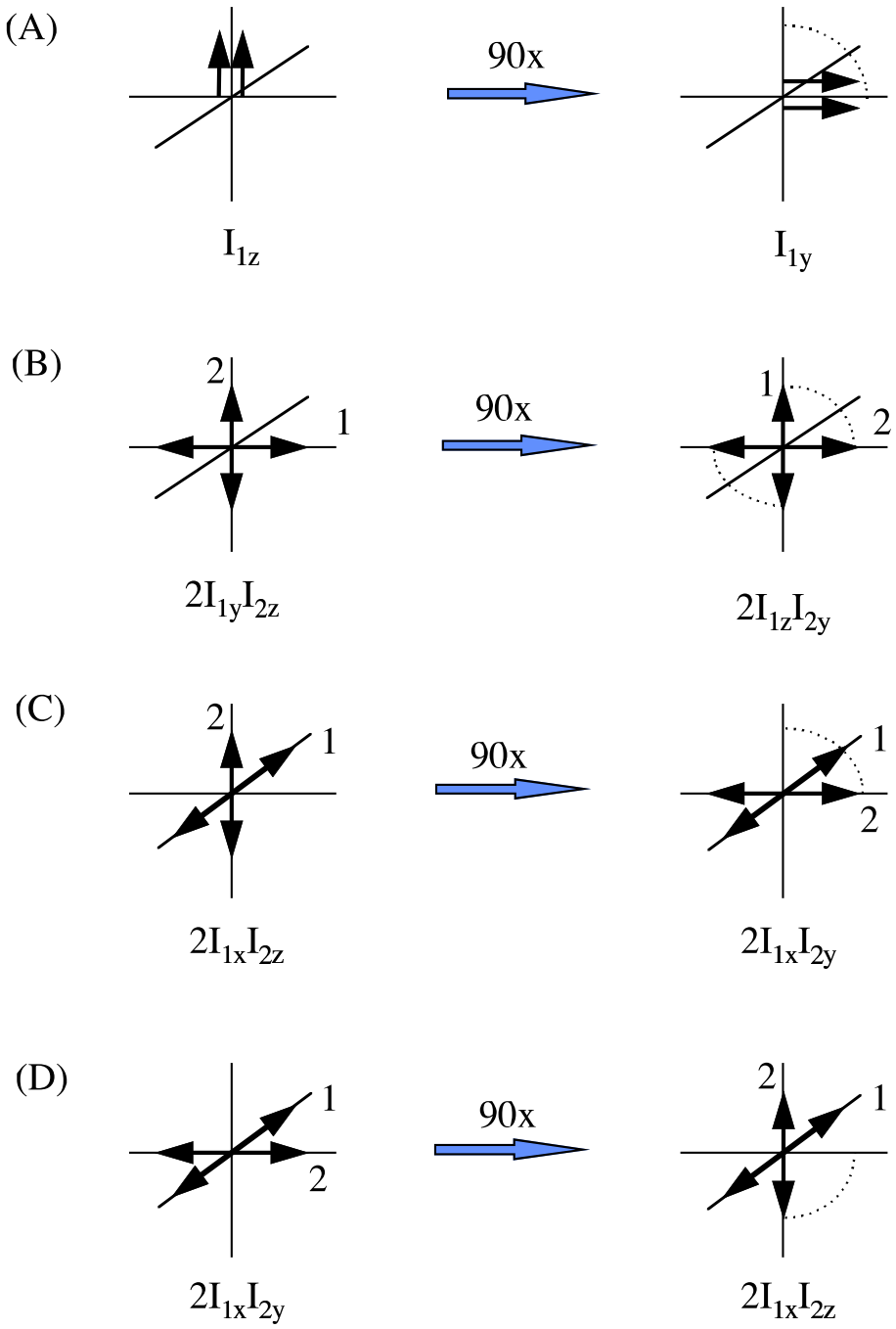

Figure 7.7: Pictorial description of the effect of 90°_x pulses. (A) Zeeman magnetization is converted to single quantum coherence by a 90°_x pulse. (B) Antiphase vector $2I_{1y}I_{2z}$ is converted to antiphase vector $2I_{1z}I_{2y}$. Magnetization is transferred from spin 1 to spin 2. (C) Multiple quantum coherence is generated from an antiphase vector by a 90° pulse on the *x*-axis. (D) Multiple quantum coherence is converted back to single quantum coherence by a 90° pulse on the *y*-axis.

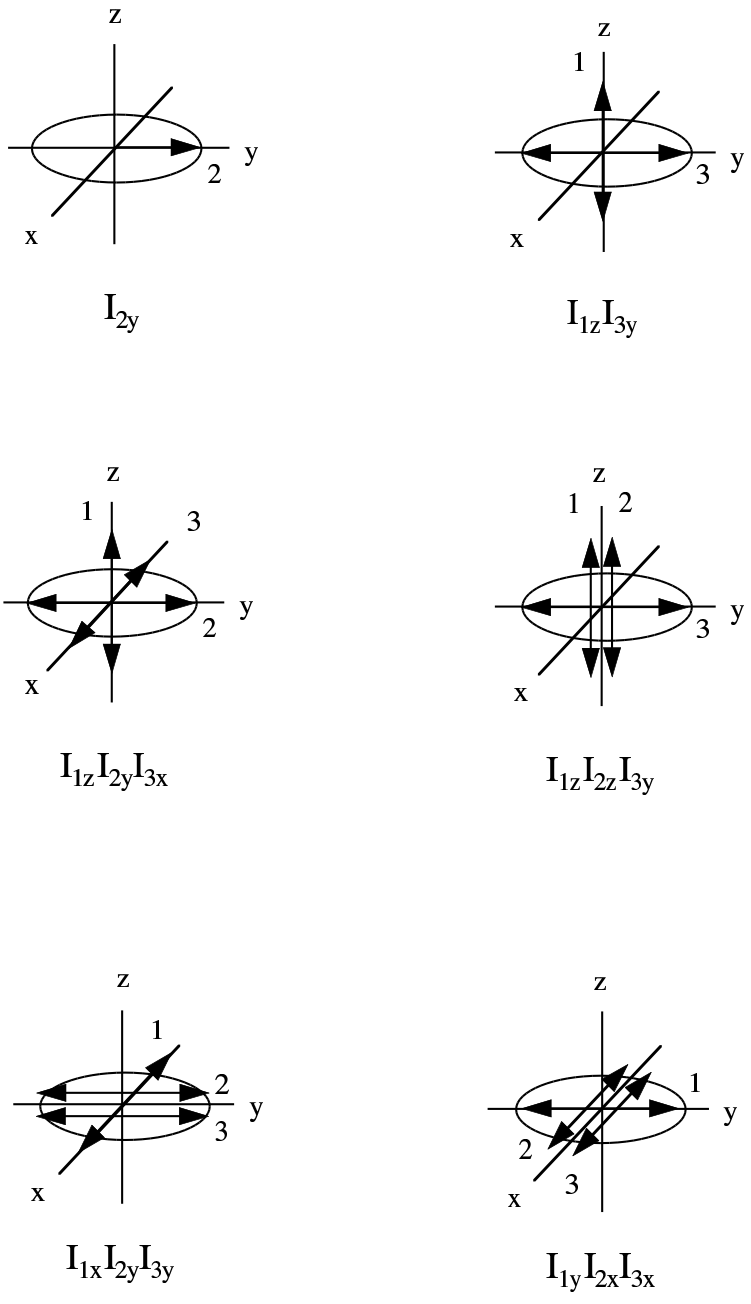

Figure 7.8: Some non-classical vectors for a three-spin system. The numerical factors for the product operators are dropped for simplicity. The in-phase components are combined (see I_{2y}) and antiphase relationship among spins is emphasized.

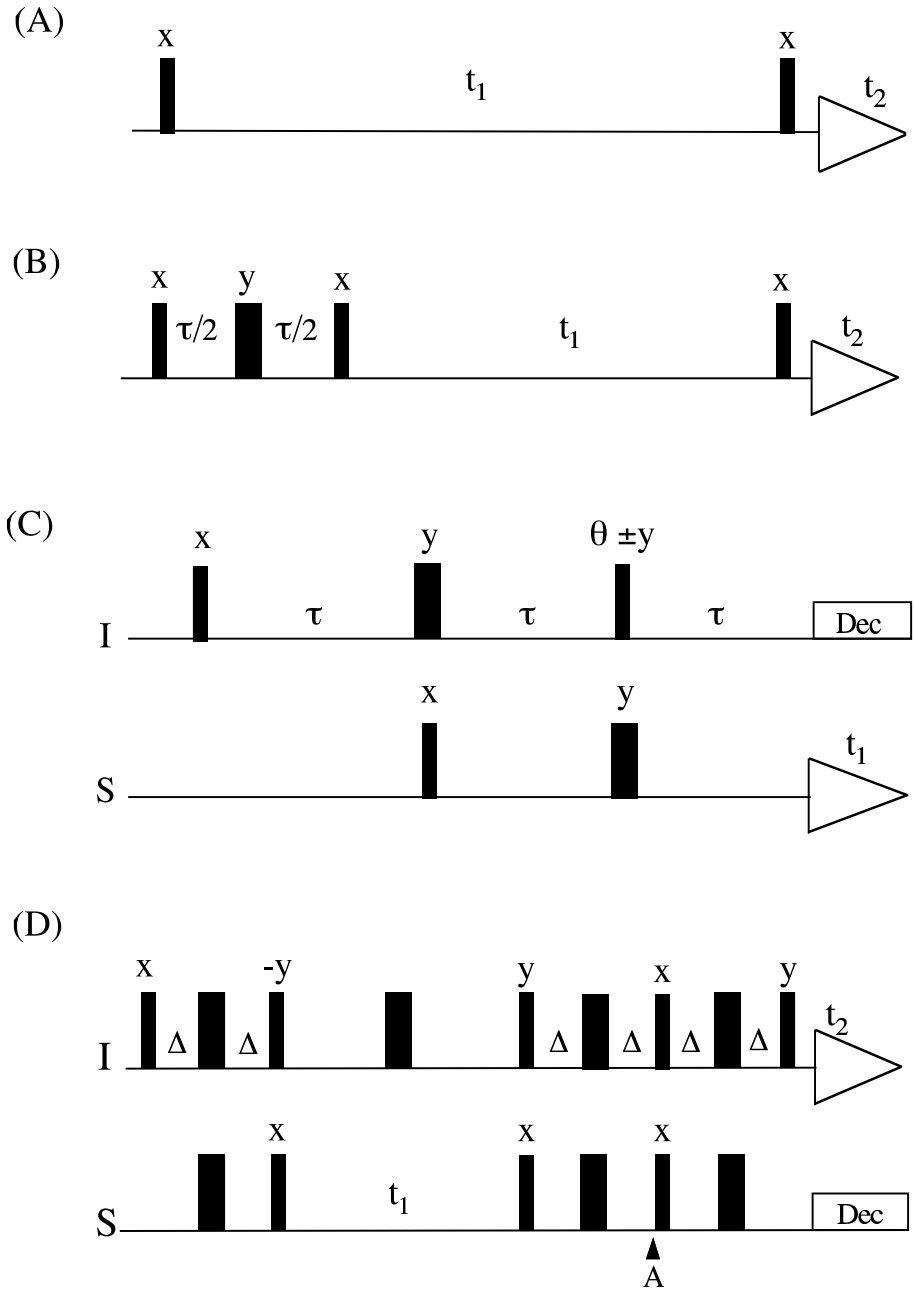

Figure 7.9: Pulse sequences of COSY (A), INADEQUATE (B), DEPT (C), and 2D sensitivity-enhanced HSQC (D). The pulse flip angles ($\pi/2$ or π) are distinguished by the pulse widths. The pulse phases are indicated for the first transient of the phase cycle for each experiment. All 180° pulses in (D) are applied on the *y*-axis.

7.4.1 Coherence transfer: the 2D COSY experiment

The homonuclear COSY experiment is one of the most important experiments in modern NMR and the first 2D experiment described. Its pulse sequence is so elegantly simple, and yet the underlying process cannot be understood using classical magnetization arguments. The pulse sequence is shown in Figure 7.9A. The new vector description of COSY for two weakly-coupled spins is shown in Figure 7.10. We start from *z*-magnetization from spin 1 on the *z*-axis. One half of the population difference corresponds to the α state of spin 2 and the other half corresponds to the β state of spin 2. A 90°_x pulse will tip the magnetization to the *y*-axis. Chemical shift evolution of spin 1 at angular frequency ω_1 during t_1 will rotate the magnetization to a new position as shown in Figure 7.10A. Now we decompose the magnetization into *x*-component labeled (a) and *y*-component labeled (b) and follow their fate separately. Under *J*-coupling, the *x*-component (a) gives an in-phase magnetization (c) with cosine modulation and an antiphase magnetization (d) with sine modulation. Note that for antiphase vector (d), the transverse magnetization is on spin 1 throughout the evolution time t_1.

Origin of diagonal peaks

In Figure 7.10B, the details beginning from the second 90°_x pulse is given for in-phase magnetization vector (c). The second 90°_x pulse will not affect the magnetization along *x*-axis. During acquisition time t_2, scalar coupling will again give rise to an in-phase vector and an antiphase vector. The chemical shift ω_1 modulation of the in-phase vector will give an observable signal on spin 1 during acquisition. This is the origin of diagonal peaks in the COSY experiment, because the magnetization resides in spin 1 during both the evolution time t_1 and the acquisition time t_2. The final antiphase vectors derived from antiphase vector (g) in Figure 7.10B do not give any observable signals.

Origin of cross peaks

The origin of cross peaks in COSY is detailed in Figure 7.10C. The antiphase vector (d) from Figure 7.10A is converted to another antiphase vector (h) by the second 90°_x pulse. The difference between the two is that before the second 90°_x pulse the transverse magnetization is on spin 1 and modulated by the chemical shift frequency ω_1 during t_1 evolution whereas the transverse magnetization is on spin 2 and modulated by the chemical shift frequency ω_2 after the second 90°_x pulse. This is the mixing step in COSY. Scalar coupling will then give rise to in-phase vector (i) and antiphase vector (j). The in-phase vector (i) will lead to detectable magnetization modulated by the chemical shift frequency of ω_2. The final antiphase vectors derived from antiphase vector (j) are again unobservable. Because the detectable vector is modulated by the chemical shift frequency ω_1 during evolution and by chemical shift frequency ω_2 during acquisition, cross peaks will be obtained.

Phase properties of COSY peaks

In a COSY spectrum of a weakly-coupled spin system, the phases of the diagonal peaks and the cross peaks differ by 90°. This feature of the COSY experiment can be visualized in the vector diagrams. The diagonal peaks are derived from the in-phase vector (e) in Figure 7.10B and the

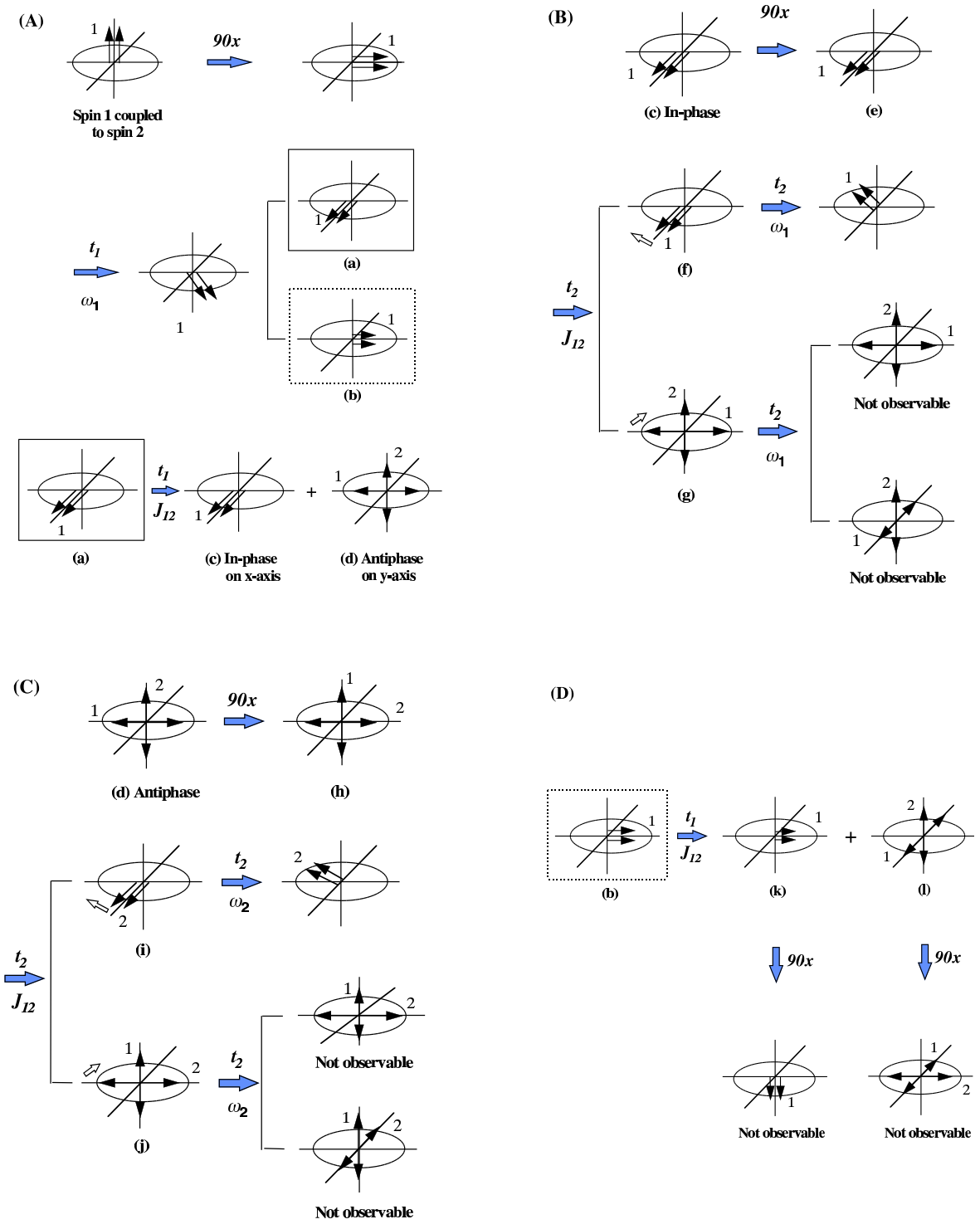

Figure 7.10: Non-classical vector description of the COSY experiment. (A) Generation of in-phase (c) and antiphase (d) components in the COSY experiment. (B) Fate of in-phase vector (c): origin of diagonal peaks. (C) Fate of antiphase vector (d): origin of cross peaks. (D) Zeeman magnetization and multiple quantum coherence derived from in-phase vector (b) are not directly observable. See text for details.

cross peaks from the antiphase vector (h) in Figure 7.10C immediately after the second 90° pulse. At the beginning of t_2, vector (e) is on the *x*-axis while vector (h) is on the *y*-axis. Therefore a 90° phase difference is expected between the diagonal peaks and the cross peaks. In practice, cross peaks are usually phased to absorptive mode, while the diagonal peaks are necessarily in the dispersive mode. Furthermore, because diagonal peaks are derived from the in-phase vector (e) and cross peaks are derived from the antiphase vector (h), we get in-phase pairs for components of the multiplets for the diagonal peaks and antiphase pairs for components of the multiplets for the cross peaks for an AX spin system in a COSY experiment.

The unobservable coherence

Finally, Figure 7.10D shows what happens to the *y*-component (b) in Figure 7.10A. Scalar coupling during evolution will lead to in-phase vector (k) and antiphase vector (l). Then in-phase vector (k) is converted to Zeeman magnetization by the second 90°_x pulse and becomes unobservable. Antiphase vector (l) is converted to multiple quantum coherence (in this case double-quantum and zero-quantum coherence) and is not observable during acquisition. The unobservable coherence shown here is actually the origin of sensitivity enhancements in many multidimensional NMR experiments, in which the unobservable coherence is converted to observable magnetization by adding additional pulses in those experiments, a topic that will be visited in more detail later. This also illustrates an important aspect in multiple pulse NMR: different coherence pathways will experience different effects in multiple pulse experiment. When a specific pathway gives rise to undesired signals, it has to be suppressed either by phase cycling or dephased by pulsed field gradients.

7.4.2 Multiple-quantum coherence spectroscopy

In multi-dimensional NMR, multiple quantum processes are more the rule than the exception. Multiple quantum filters are used to suppress single-quantum diagonal peaks in Double-quantum-filtered COSY (DFQ-COSY) experiment. Multiple quantum coherence evolution is present in a number of indirect detection experiments such as HMQC and many triple-resonance experiments. Here we present the vector description of INADEQUATE-2D (Incredible Natural Abundance DoublE QUantum Transfer Experiment) [14-16], which is mainly used for the correlation of ^{13}C nuclei in organic molecules. The basic pulse sequence is shown in Figure 7.9B.

The INADEQUATE experiment

In the INADEQUATE experiment, the spin system of interest is the isolated coupled ^{13}C pairs present in natural abundance sample. In a weakly-coupled two-spin (^{13}C) system, the magnetization is along the *z*-axis at equilibrium. In Figure 7.11A, only in-phase magnetization from spin C1 is shown. The first 90°_x pulse will rotate the in-phase magnetization into *xy*-plane. Antiphase magnetization on C1 will develop to its maximum amplitude during time $\tau = 1/2J$ and the magnitude of the in-phase component will be zero due to scalar coupling between C1 and C2. The 180°_x pulse in the middle will refocus chemical shift evolution during τ and is not explicitly included in the vector diagram. The second 90°_x pulse converts the antiphase magnetization on spin C1 to multiple-quantum coherence (magnetization vectors for both C1 and C2 are now within the *xy*-plane). Then

the multiple quantum vector will evolve during t_1 to give four vector terms (Figures 7.11A (a)-(d), also see Figure 7.5B). The third 90°_x pulse converts the first two vectors (a) and (b) into observable single quantum magnetization (Figure 7.11A (e) and (f)) for detection. Specifically, vector (e) will give resonances at $(\omega_1+\omega_2, \omega_1)$ and vector (f) will give resonances at $(\omega_1+\omega_2, \omega_2)$. Note that the multiple quantum coherence present during t_1 evolution is a mixture of double- and zero-quantum coherence. Because of the phase cycling scheme used, only double-quantum coherence is selected during the t_1 evolution time while zero-quantum coherence is suppressed by phase cycling. Therefore the effective chemical shift evolution frequency is the sum of the chemical shift frequencies of the two spins involved. It can be readily seen that during the evolution time t_1, the chemical shift evolution from both C1 and C2 are in effect because both vectors are within the *xy*-plane, while during acquisition, only one magnetization vector from either C1 (Figure 7.11A (e)) or C2 (Figure 7.11A (f)) is within the *xy*-plane. This leads to a cross peak at $\omega_1+\omega_2$ in $F1$ and ω_1 or ω_2 in F2. In Figure 7.11A (g) and (h), the vectors represent Zeeman and multiple quantum coherence and are not directly detectable.

The importance of phase cycling

The success of the original INADEQUATE experiment relies heavily on phase cycling to suppress signal from uncoupled ^{13}C nuclei present in the sample (about 100 times more intense as the desired signal) and signal from other unwanted pathways. To illustrate the importance of phase cycling, we present the fate of uncoupled ^{13}C spins in Figure 7.11B as an example. The equilibrium magnetization of the uncoupled spin C1 is rotated to the *xy*-plane by the first 90°_x pulse. No net chemical shift evolution or scalar coupling evolution is present during delay τ (the 180° pulse refocuses chemical shift evolution during the delay τ). The second 90°_x pulse converts the transverse magnetization to Zeeman magnetization. After the evolution time, the last 90°_x pulse will again convert the Zeeman magnetization to transverse magnetization. This magnetization will be detected if not suppressed by phase cycling or alternatively by pulsed-field gradients. For the INADEQUATE experiment, a minimum of 4-step phase cycling is sufficient to select double quantum coherence while suppressing zero- and single-quantum coherence during evolution time t_1. It can be clearly seen now that coherence selection (and suppression of unwanted coherence pathways) is indispensable in multidimensional NMR experiments. The principles involved in coherence selection by phase cycling have been elegantly described in the literature [19,20]. The details of phase cycling as applied to DQF-COSY have been illustrated by Shriver [9]. The basic principle of coherence selection by phase cycling can be summarized as follows: the NMR signal derived from a particular pathway has a specific phase factor associated with the signal. When signals from a complete phase cycle are combined, the signal from different scans will add up for the desired pathway(s), while signal from different scans will sum to zero for the unwanted pathways.

Finally, if the tip-angle of the last pulse is not 90°, then all vectors represented by (a), (b), (c), and (d) will more or less contribute to the signal detected, leading to different pathways to be selected. A comprehensive analysis is best done using product operator formalism. However, a qualitative understanding of the tip-angle effect is still possible if all four vectors before the final pulse are considered.

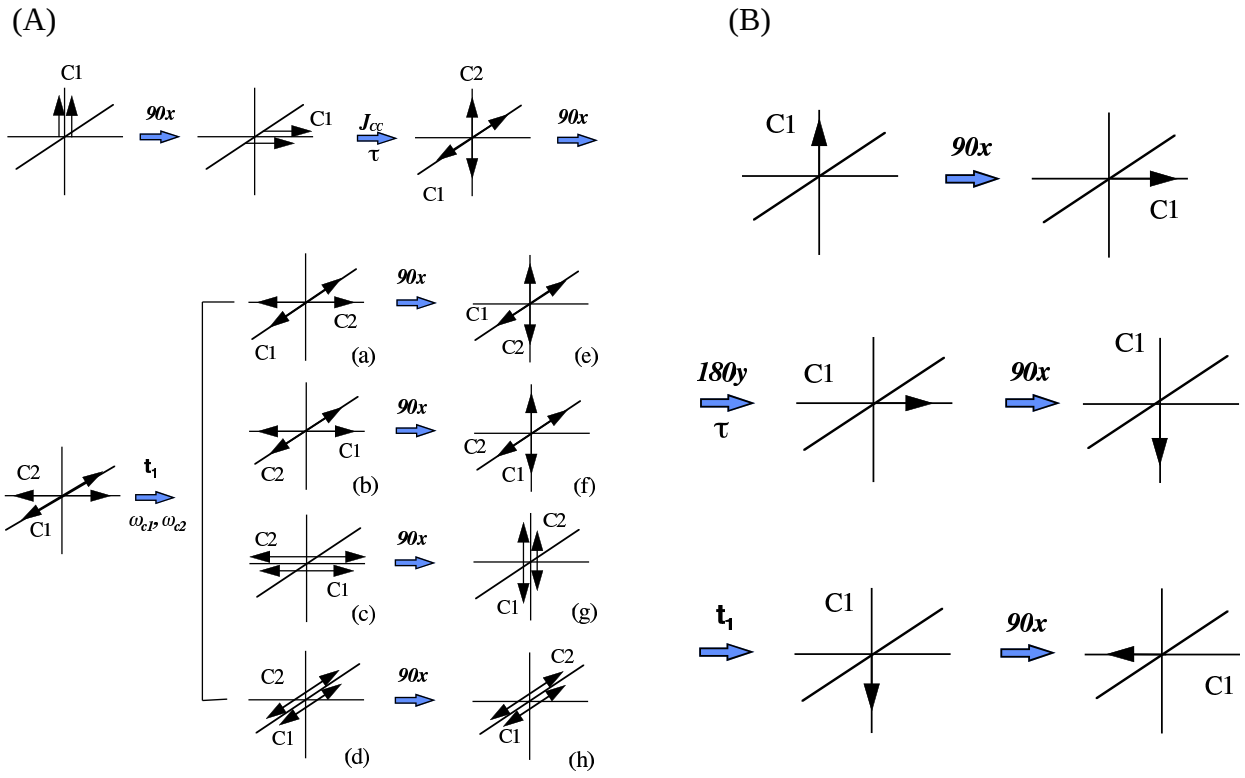

Figure 7.11: Non-classical vector diagrams for the INADEQUATE experiment. (A) In-phase magnetization is allowed to evolve under scalar coupling during delay τ. At the end of delay τ, the anti-phase vector is at its maximum amplitude. Multiple quantum evolution takes place during evolution time t_1, giving rise to four multiple quantum vectors shown in (a), (b), (c), and (d). The last 90° pulse converts multiple quantum vectors (a) and (b) into observable magnetization for detection. Vectors (c) and (d) remain unobservable. (B) Uncoupled ^{13}C nuclei will contribute to detected signal if not suppressed by phase cycling or dephased by pulsed-field gradients. The minimum phase cycle to select double-quantum coherence during t_1 while suppressing single-quantum and zero-quantum coherence is a four step cycle for the first three pulses in the sequence.

The DEPT experiment

Another representative experiment that makes use of multiple quantum coherence is the DEPT experiment (Distortionless Enhancement by Polarization Transfer) [17,18]. The pulse sequence of the experiment is shown in Figure 7.9C. The simple case of a two-spin *IS* system with one proton coupled to heteroatom ^{13}C will be considered here. For simplicity the chemical shift evolution of the *I* spin during the first 2τ delay and the *S* spin during the last 2τ delay will not be included in the vector diagrams. The chemical shift evolution is refocused by the 180° pulses in the middle of the two delays, respectively. The first 90° pulse on *I* (proton) rotates the ^{1}H magnetization vector (a) into the *xy*-plane. Under scalar coupling between ^{13}C and ^{1}H, the ^{1}H in-phase vector (b) is completely converted to antiphase vector (c) when the delay τ is set to $1/(2J_{CH})$. The first ^{13}C 90° pulse on the *x*-axis will then generate the desired multiple quantum vector (d). The multiple quantum vector does not evolve under active scalar coupling and is in a sense frozen during the following τ delay (Figure 7.6C). At the end of the second τ delay the multiple quantum vector (d) is converted to vector (e) by the last ^{1}H pulse with tip-angle θ. Vector (e) can then be decomposed into an antiphase vector (f) (with a sine amplitude dependence on θ) and multiple quantum vector (g) (with a cosine amplitude dependence on θ). From antiphase vector (c) to antiphase vector (f), the magnetization from ^{1}H in (c) is transferred to ^{13}C in (f). The anti-phase vector (f) then evolves into in-phase vector (h) during the last τ delay for observation. The "Distortionless" in DEPT comes from the fact that the observable magnetization at the start of acquisition is in-phase as opposed to antiphase in INEPT and broadband decoupling can be applied on the *I* spin (proton) during acquisition. The multiple quantum vector (g) decomposed from vector (e) does not evolve under active *J*-coupling and remains unobservable.

One important feature of the DEPT experiment is that the magnitude of the observable in-phase vector (h) derived from vector (f) depends on the tip-angle θ of the last proton pulse. For CH groups, the magnitude of the observable magnetization is sine-dependent on θ as shown by vector (e) in Figure 7.12. For CH_2 and CH_3 groups the tip-angle dependence is different (it is $\sin\theta\cos\theta$ for CH_2 groups and $\sin\theta\cos^2\theta$ for CH_3 groups, see references [17,18]). Therefore signals from CH, CH_2, and CH_3 can be easily separated by suitable linear combinations of spectra obtained with different values of θ. The sign of the last *I* pulse is inverted in alternate experiments and the resulting FIDs are stored in subtractive combination to eliminate the native *S* magnetization not shown in the vector diagrams.

7.4.3 Sensitivity enhancement in multidimensional NMR

NMR spectroscopy is one of the most powerful techniques in the studies of structure, dynamics, and interactions of biomolecules. Unfortunately, it is also a very insensitive technique compared to other spectroscopic methods in terms of the achievable signal-to-noise ratio per unit measuring time. The problem is worse in multidimensional NMR spectroscopy due to the fact that each time the spectral dimensionality is increased, the sensitivity drops by a factor of $\sqrt{2}$ because the real and imaginary components of the signal must be sampled in separate experiments. As a result the optimization of sensitivity of multidimensional NMR experiments is a very important area of research and development In recent years an ingenious approach that falls into the spin physics modification category has been proposed by Rance and coworker [21, 22] to enhance the sensitivity of a number of 2D experiments by a factor of $\sqrt{2}$ and has been extended to three-dimensional

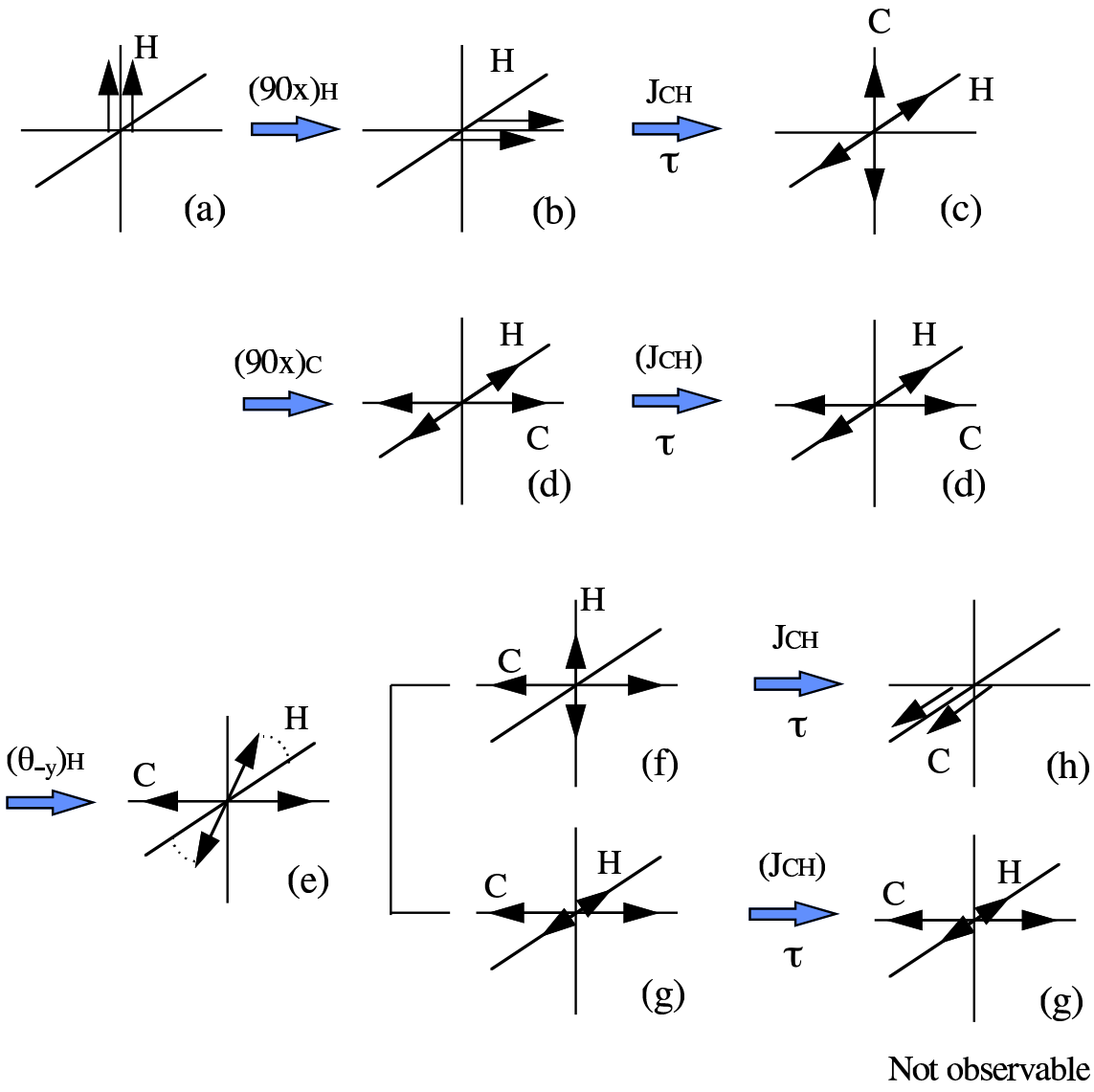

Figure 7.12: Non-classical vector diagrams of the DEPT experiment for a two-sin system *IS* with one proton coupled to ^{13}C. After the first ^{1}H pulse the in-phase ^{1}H vector is converted to antiphase vector due to scalar coupling between ^{13}C and ^{1}H. A 90° pulse on ^{13}C on the *x* axis generates the desired multiple quantum vector. This multiple quantum vector is frozen until the last ^{1}H pulse with a tip-angle of θ is applied. Then multiple quantum vector is partially converted to an antiphase vector, from which the observable in-phase vector is derived. The delay τ is set to $1/(2J_{CH})$ to maximize the magnitude of the antiphase and multiple quantum vectors. The two 180° pulses will refocus chemical shift evolution of *I* spin (during the first 2τ delay) and *S* spin (during the last 2τ delay) respectively and are not included in the diagrams.

experiment [23]. A gradient version of the 2D sensitivity-enhanced HSQC experiment has been reported by Kay et al. to achieve the same goal [24] and has been incorporated into many recent 3D triple-resonance experiments for labeled proteins [25]. In this section, the principles involved in this class of sensitivity-enhanced experiments will be described by non-classical vectors using the original sensitivity-enhanced HSQC experiment as an example.

Sensitivity enhancement and quadrature detection

The sensitivity enhancement found in the Rance-type experiments are closely related to quadrature phase-sensitive detection and cross-coil detection in one-dimensional NMR to achieve $\sqrt{2}$ improvements in sensitivity. For quadrature detection in 1D experiments, the signal intensity is twice as that in single phase-sensitive detection because the *x*- and *y*-magnetization are detected at the same time. In two-dimensional NMR experiments, the quadrature detection with pure absorption in the indirect dimension is invariably implemented so that the cosine- and sine-modulated signals (analogous to the *x*- and *y*-magnetization in the 1D experiment) are recorded in two separate experiments. Therefore a $\sqrt{2}$ loss in sensitivity will occur each time the dimensionality of the experiment is increased. In the sensitivity enhanced experiments this problem is solved by modifying the spin physics of the experiment to simultaneously detect both components in the indirect dimension. The details of sensitivity enhancement are illustrated below using the HSQC experiment [22] as an example.

The original HSQC experiment

The pulse sequence of the sensitivity-enhanced HSQC experiment is shown in Figure 7.9D. The sequence of the normal HSQC includes all pulses up to point A in Figure 7.9D. The vector description of the normal HSQC experiment is shown in Figure 7.13A. Starting from thermal equilibrium, the Zeeman magnetization of spin I (^{1}H) is tipped down to the *xy*-plane by the first 90° pulse, creating coherence on spin I. During the next 2Δ delay the net active evolution comes from scalar-coupling between spin I and S, with chemical shift evolution refocused by the 180° pulse on spin I. Because $2\Delta = 1/(2J_{IS})$ the magnitude of the antiphase vector is at its maximum and the magnitude of in-phase vector is zero and is not shown. The 90° pulses on both I and S transfer spin coherence from spin I to spin S, setting the stage for frequency labeling of the heteronucleus during t_1. During t_1 the J-coupling between spins I and S is decoupled by the 180° pulse on spin I at the middle of t_1 and need not be considered. Chemical shift evolution of antiphase vector $2I_zS_y$ gives two new antiphase vectors $2I_zS_y\cos\omega_S t_1$ and $2I_zS_x\sin\omega_S t_1$ (see also Figure 7.5B). The two 90° pulses on both I and S transfer magnetization in antiphase vector $2I_zS_y$ from spin S to spin I, generating antiphase vector $2I_yS_x$ with coherence present on spin I. The other antiphase vector at the end of t_1 is now converted to multiple-quantum vector by the two 90° pulses. During the subsequent 2Δ delay with the heteronuclear scalar-coupling active, the antiphase vector evolves into observable in-phase vector. And the multiple quantum vector does not change under the influence of active coupling (see also Figure 7.5C). Note that in the normal HSQC experiment, only the in-phase vector at the end of Figure 7.13A contributes to observable signal. The boxed vector represents multiple quantum coherence and is not directly observable.

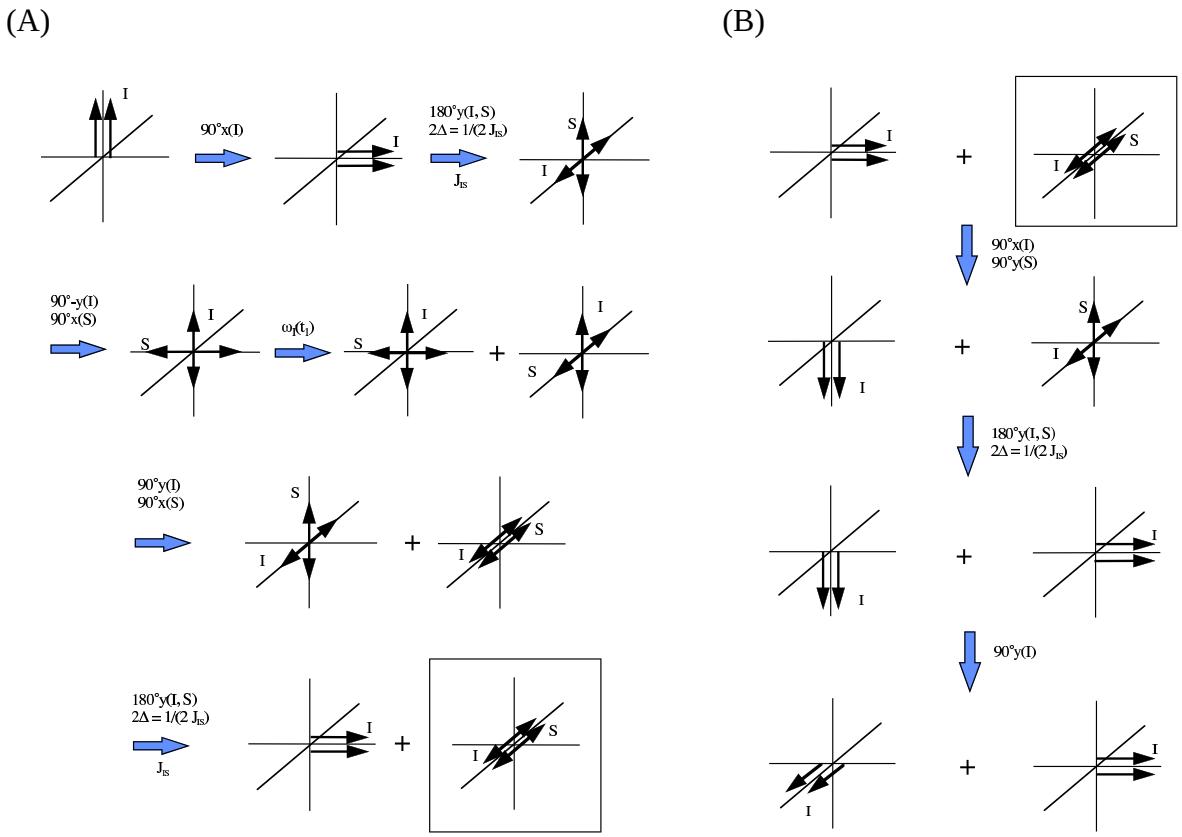

Figure 7.13: Non-classical vector description of sensitivity enhancement in 2D sensitivity-enhanced HSQC. (A) Vector description of the normal HSQC experiment. (B) Vector description of sensitivity improvement in sensitivity-enhanced HSQC.

The sensitivity-enhanced HSQC experiment

For the sensitivity enhanced experiment, the evolution up to point A indicated by the arrow in Figure 7.9D is identical to the normal HSQC experiment. The key to the sensitivity enhancement is the additional pulses and evolution period after point A. At the end of the normal HSQC pulse sequence, only the in-phase I-vector is observable, the multiple-quantum vector does not contribute to observable signal. As shown in Figure 7.13, the in-phase I-vector is first converted to Zeeman magnetization by the 90° pulse on I-spin and stored as z-magnetization. The multiple quantum vector is first converted into antiphase I vector. In the $2\Delta = 1/(2J_{IS})$ delay, the antiphase vector has evolved into in-phase I-vector due to J-coupling. No evolution takes place for the z-magnetization for the I-spin during 2Δ. Finally, the z-magnetization is rotated to the x-axis, giving two observable vectors (one on the x axis and and the other on the y-axis) at the same time. The net result is that the multiple quantum vector in the normal HSQC experiment has been converted into observable in-phase I vector and the intrinsic sensitivity of the experiment has been enhanced. The increase by a factor of $\sqrt{2}$ comes from the fact that the x vector is sine modulated in t_1 and the y-vector is cosine modulated in t_1, giving a 90° phase difference between the two signals in t_1. The vector sum of the two signals in the indirect dimension then gives a $\sqrt{2}$ increase in sensitivity. The sensitivity improvement is identical with that obtained in quadrature detection compared to single-channel detection in 1D experiments.

7.5 Conclusion

In this chapter we have presented a complete non-classical vector model for the product-operator formalism. Using this model any multi-dimensional NMR experiments can be visualized in a traditional hand-waving manner. The derivation of the new vectors has been discussed in detail and the time evolution of product operator has also been presented. Examples are given for this new vector model. It is hoped that this new vector model will be useful in understanding complicated multi-pulse multi-dimensional NMR experiments without resorting to the product operator formalism itself and provide a useful teaching tool for the biophysics community.

7.6 References

1. R. Benn and H. Günther, "Modern pulse methods in high-resolution NMR spectroscopy," *Angew. Chem. Int. Ed. Engl.*, **1983**, *22*, 350–380.

2. A. Abragam, *The Principles of Nuclear Magnetism*, Oxford University Press, London, 1963, pp. 1–599.

3. C. Slichter, *Principles of Magnetic Resonance*, 2nd Ed. Springer-Verlag, New York, 1990, pp. 1–655.

4. M. Goldman, *Quantum Description of High-Resolution NMR in Liquids*, Clarendon Press, Oxford, 1990, pp. 1-268.

5. R. R. Ernst, G. Baudenhausen, and A. Wokaun, *Principles of Nuclear Magnetic Resonance in One and Two Dimensions*, Clarendon Press, Oxford, 1987, pp. 1–610.

6. O. W. Sørensen, G. W. Eich, M. H. Levitt, G. Bodenhausen, and R. R Ernst, "Product operator formalism for the description of NMR pulse experiments," *Prog. Nucl. Magn. Reson. Spectrosc.*, **1983**, *16*, 163–192.

7. H. Kessler, M. Gehrke, and C. Griesinger, "Two-dimensional NMR spectroscopy: Background and overview of experiments," *Angew. Chem. Int. Engl. Ed.*, **1988**, *27*, 490–536.

8. R. Bazzo, J. Boyd, I. D. Campbell, and N. Soffe, "A diagrammatic representation of both in-phase and antiphase coherence transfer processes with a simple application," *J. Magn. Reson.*, **1987**, *73*, 369–374.

9. J. Shriver, "Product operators and coherence transfer in multiple pulse NMR experiments," *Concepts Magn. Reson.*, **1992**, *4*, 1–33.

10. G. Wei and R. F. Snider, "A pictorial representation for multispin evolutions," *Concepts Magn. Reson.*, **1995**, *7*, 153–163.

11. D. F. Lowry, "Correlated vector model of multiple-spin systems," *Concepts Magn. Reson.*, **1994**, *6*, 25–39.

12. D. G. Donne and D. G. Gorenstein, "A pictorial representation of product operator formalism: nonclassical vector diagrams for multidimential NMR," *Concepts Magn. Reson.*, **1997**, *9*, 95–111.

13. W. P. Aue, E. Bartholdi, and R. R. Ernst, "Two-dimensional spectroscopy. Application to nuclear magnetic resonance," *J. Chem. Phys.*, **1976**, *64*, 2229–2246.

14. A. Bax, R. Freeman, S. P. Kempsell, "Natural abundance ^{13}C-^{13}C coupling observed via double-quantum coherence," *J. Am. Chem. Soc.*, **1980**, *102*, 4849–4851.

15. A. Bax, R. Freeman, and T. Frenkiel, "An NMR technique for tracing out the carbon skeleton of an organic molecule," *J. Am. Chem. Soc.*, **1981**, *103*, 2102–2104.

16. R. Freeman, T. Frenkiel, and M. B. Rubin, "Structure of a photodimer determined by natural-abundance ^{13}C-^{13}C coupling," *J. Am. Chem. Soc.*, **1982**, *104*, 5545–5547.

17. D.M. Dodrell, D.T. Pegg, and M.R. Bendall, "Distortionless enhancement of NMR signals by polarization transfer," *J. Magn. Reson.*, **1982**, *48*, 323–327.

18. M.R. Bendall, and D.T. Pegg, "Complete accurate editing of decoupled ^{13}C spectra using DEPT," *J. Magn. Reson.*, **1983**, *53*, 272–296.

19. G. Bodenhausen, H. Kogler, and R. R. Ernst, "Selection of coherence transfer pathways in NMR pulse experiments," *J. Magn. Reson.*, **1984**, *58*, 370–388.

20. A. D. Bain, "Coherence levels and coherence pathways in NMR: A simple way to design phase cycling procedures," *J. Magn. Reson.*, **1984**, *56*, 418–427.

21. J. Cavanagh and M. Rance, "Sensitivity Improvement in isotropic mixing (TOCSY) experiments," *J. Magn. Reson.*, **1990**, *88*, 72–85.

22. A. G. Palmer III, J. Cavanagh, P. E. Wright, and M. Rance, "Sensitivity improvement in proton-detected two-dimensional heteronuclear correlation NMR spectroscopy," *J. Magn. Reson.*, **1991**, *93*, 151–171.

23. A. G. Palmer III, J. Cavanagh, P. E. Wright, and M. Rance, "Sensitivity improvement in three-dimensional heteronuclear correlation NMR spectroscopy," *J. Magn. Reson.*, **1992**, *96*, 416–424.

24. L. E. Kay, P. Keifer, and T. Saarinen, "Pure absorption gradient enhanced heternuclear single quantum correlation spectroscopy with improved sensitivity," *J. Am. Chem. Soc.*, **114**, 10663–10665.

25. D. R. Muhandiram and L. E. Kay, "Gradient-enhanced triple-resonance three-dimensional NMR experiments with improved sensitivity," *J. Magn. Reson.*, **1994**, *B 103*, 203–216.